

# **An Atlas of Accessible Chromatin in Advanced Prostate Cancer Reveals the Epigenetic Evolution during Tumor Progression**

**Raunak Shrestha<sup>1,2</sup>, Lisa N. Chesner<sup>1,2</sup>, Meng Zhang<sup>1,2</sup>, Stanley Zhou<sup>3,4</sup>, Adam Foye<sup>1,5</sup>, Arian Lundberg<sup>1,2,6</sup>, Alana S. Weinstein<sup>1,2</sup>, Martin Sjöström<sup>1,2</sup>, Xiaolin Zhu<sup>1,5</sup>, Thaidy Moreno-Rodriguez<sup>1,7</sup>, Haolong Li<sup>1,2</sup>, SU2C/PCF West Coast Prostate Cancer Dream Team<sup>\*</sup>, Joshi J. Alumkal<sup>8</sup>, Rahul Aggarwal<sup>1,5</sup>, Eric J. Small<sup>1,2,5,7</sup>, Mathieu Lupien<sup>3,4,9,†</sup>, David A. Quigley<sup>1,7,10,†</sup>, and Felix Feng<sup>1,2,5,7,†</sup>**

<sup>1</sup>Helen Diller Family Comprehensive Cancer Center, University of California, San Francisco, San Francisco, CA, USA

<sup>2</sup>Department of Radiation Oncology, University of California, San Francisco, San Francisco, CA, USA

<sup>3</sup>Princess Margaret Cancer Centre, University Health Network, Toronto, ON, Canada

<sup>4</sup>Department of Medical Biophysics, University of Toronto, Toronto, ON, Canada

<sup>5</sup>Division of Hematology and Oncology, Department of Medicine, University of California, San Francisco, San Francisco, San Francisco, CA, USA

<sup>6</sup>The Institute of Cancer Research and The Royal Marsden Hospital, London, UK

<sup>7</sup>Department of Urology, University of California, San Francisco, San Francisco, CA, USA

<sup>8</sup>Division of Hematology and Oncology, University of Michigan Rogel Cancer Center, Ann Arbor, MI, USA

<sup>9</sup>Ontario Institute for Cancer Research, Toronto, ON, Canada

<sup>10</sup>Department of Epidemiology & Biostatistics, University of California, San Francisco, San Francisco, CA, USA

<sup>\*</sup>A list of members and their affiliations appears in the Supplementary Information

<sup>†</sup>These authors jointly supervised the work

## **Corresponding Author:**

Felix Y. Feng, MD, Department of Radiation Oncology, University of California, San Francisco, Box 3110, Room 450, 1450 3rd Street, San Francisco, CA 94158; Phone: 415-502-7222; E-mail: Felix.Feng@ucsf.edu

## **Supplementary Materials**

## List of Figures

Supplementary Fig. S1	Overview of metastatic biopsy sites analyzed in this study . . . . .	4
Supplementary Fig. S2	Schematic diagram illustrating ATAC-seq data processing workflow . . . . .	5
Supplementary Fig. S3	ATAC-seq quality control metrics of the mCRPC samples . . . . .	6
Supplementary Fig. S4	Comparison of ATAC-seq quality of mCRPC samples with publicly available datasets . . . . .	7
Supplementary Fig. S5	PCA of the ATAC-seq profiles comparing different stages of prostate cancer .	8
Supplementary Fig. S6	Enrichment of accessible chromatin region in malignant prostate cancer . . . .	9
Supplementary Fig. S7	Correlation of ATAC-seq peak accessibility and corresponding RNA-seq gene expression levels . . . . .	10
Supplementary Fig. S8	Estimating ATAC-seq clusters of mCRPC samples . . . . .	10
Supplementary Fig. S9	ATAC-seq unsupervised clusters of mCRPC samples . . . . .	11
Supplementary Fig. S10	mCRPC transcriptional subtypes classification based on Labrecque et al. genelist	12
Supplementary Fig. S11	Association of ATAC-seq peaks quality metrics with mCRPC transcriptional subtypes . . . . .	13
Supplementary Fig. S12	Gene expression levels between mCRPC transcriptional subtypes . . . . .	14
Supplementary Fig. S13	Evaluation of the reliability of TF-footprint sites . . . . .	15
Supplementary Fig. S14	Percentage of TF footprint sites classified as bound and unbound . . . . .	16
Supplementary Fig. S15	Differential TF footprint occupancy between mCRPC transcriptional subtypes	17
Supplementary Fig. S16	Correlation of ATAC-seq predicted TF footprint sites with ChIP-seq peaks . .	18
Supplementary Fig. S17	Distribution of TF footprints distance to the TSS of the nearest gene . . . . .	19
Supplementary Fig. S18	Distribution of ChIP-seq peaks of mCRPC subtype associated TF . . . . .	20
Supplementary Fig. S19	Schematic workflow diagram illustrating the construction of TF-target gene regulatory network . . . . .	21
Supplementary Fig. S20	Prediction of ATAC-seq peaks potentially regulating gene expression . . . . .	22
Supplementary Fig. S21	<i>ZNF263</i> mRNA expression in prostate tissues . . . . .	23
Supplementary Fig. S22	The effects of <i>ZNF263</i> binding on its downstream target genes . . . . .	24
Supplementary Fig. S23	<i>ZNF263</i> target gene expression . . . . .	25
Supplementary Fig. S24	Association of <i>ZNF263</i> with MYC signaling pathway . . . . .	26

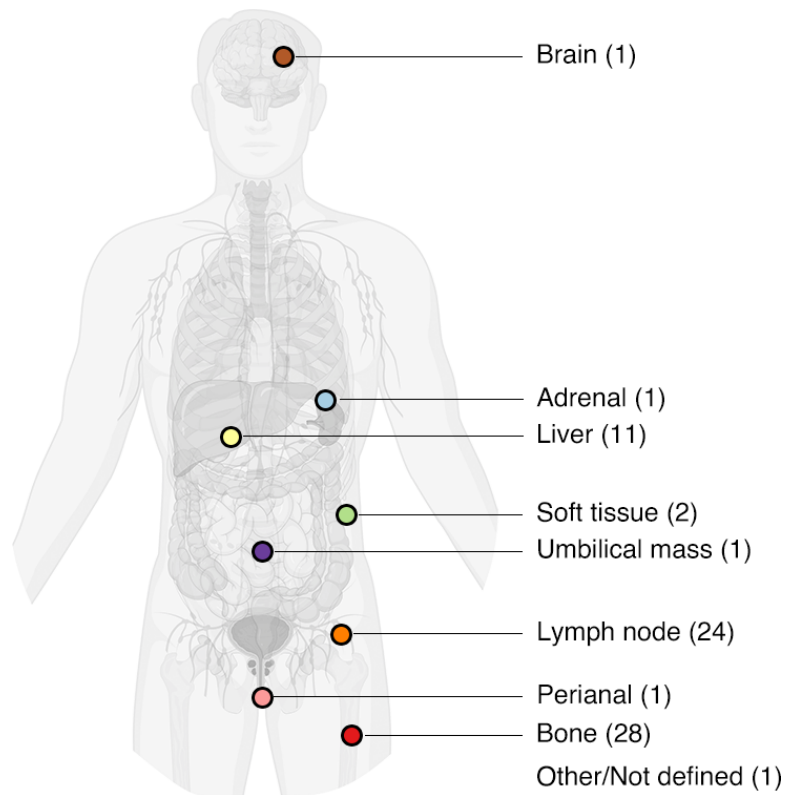
## **Stand Up 2 Cancer (SU2C) / Prostate Cancer Foundation (PCF) West Coast Prostate Cancer Dream Team**

Joshi J. Alumkal<sup>1</sup>, Tomasz M. Beer<sup>2</sup>, Kim N. Chi<sup>3,4</sup>, Christopher P. Evans<sup>5</sup>, Adam Foye<sup>6,7</sup>, Martin Gleave<sup>3</sup>, Alexander W. Wyatt<sup>3</sup>, Jiaoti Huang<sup>8</sup>, Primo N. Lara<sup>9</sup>, Robert E. Reiter<sup>10</sup>, Matthew B. Rettig<sup>11,12</sup>, George Thomas<sup>13,14</sup>, Lawrence True<sup>15</sup>, Owen Witte<sup>16</sup>, Rahul Aggarwal<sup>6,7</sup>, Eric J. Small<sup>6,7,17,18</sup>, David A. Quigley<sup>6,18,19</sup>, Felix Y. Feng<sup>6,7,17,18</sup>

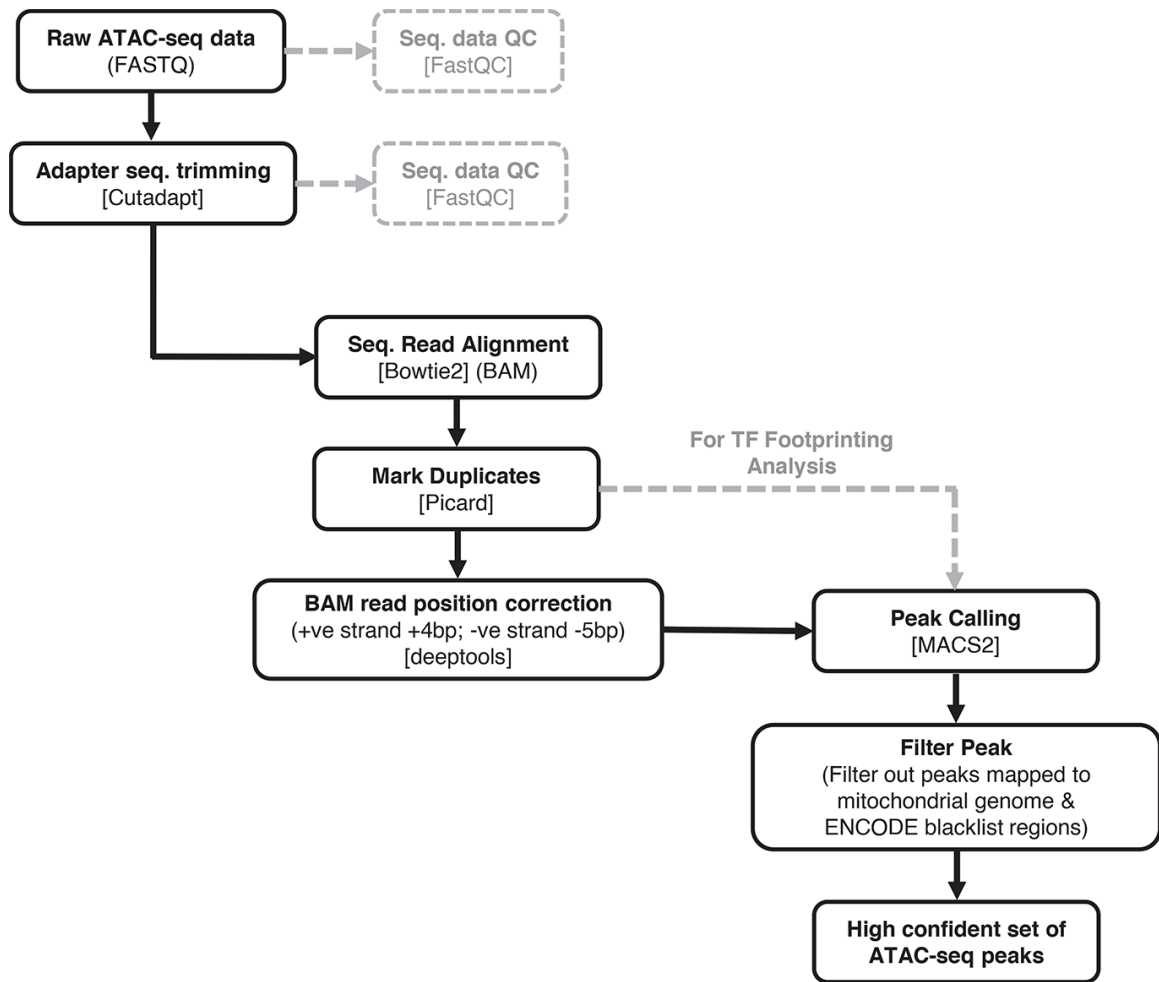
<sup>1</sup>Division of Hematology and Oncology, University of Michigan Rogel Cancer Center, Ann Arbor, MI, USA; <sup>2</sup>Knight Cancer Institute, School of Medicine, Oregon Health & Science University, Portland, OR, USA; <sup>3</sup>Vancouver Prostate Centre, Department of Urologic Sciences, University of British Columbia, Vancouver, BC, Canada; <sup>4</sup>Department of Medical Oncology, BC Cancer, Vancouver, BC, Canada; <sup>5</sup>Department of Urology, School of Medicine, University of California, Davis, Sacramento, CA, USA; <sup>6</sup>Helen Diller Family Comprehensive Cancer Center, University of California, San Francisco, San Francisco, CA, USA; <sup>7</sup>Division of Hematology and Oncology, Department of Medicine, University of California, San Francisco, San Francisco, CA, USA; <sup>8</sup>Department of Pathology, Duke University, Durham, NC, USA; <sup>9</sup>Division of Hematology and Oncology, School of Medicine, University of California, Davis, Sacramento, CA, USA; <sup>10</sup>Department of Urology, University of California, Los Angeles, Los Angeles, CA, USA; <sup>11</sup>Division of Hematology and Oncology, David Geffen School of Medicine, University of California, Los Angeles, Los Angeles, CA, USA; <sup>12</sup>Division of Hematology and Oncology, VA Greater Los Angeles Healthcare System, Los Angeles, CA, USA; <sup>13</sup>Knight Cancer Institute, Oregon Health & Science University, Portland, OR, USA; <sup>14</sup>Department of Pathology, Oregon Health & Science University, Portland, OR, USA; <sup>15</sup>Department of Pathology, University of Washington, Seattle, WA, USA; <sup>16</sup>Department of Microbiology, Immunology, and Molecular Genetics, David Geffen School of Medicine, University of California Los Angeles, Los Angeles, CA, USA; <sup>17</sup>Department of Radiation Oncology, University of California, San Francisco, San Francisco, CA, USA; <sup>18</sup>Department of Urology, University of California, San Francisco, San Francisco, CA, USA; <sup>19</sup>Department of Epidemiology & Biostatistics, University of California, San Francisco, San Francisco, CA, USA.

**SU2C / PCF West Prostate Cancer Coast Dream Team representative contact:** Dr. Felix Y. Feng, Helen Diller Family Comprehensive Cancer Center, University of California San Francisco, 1450 3rd St, Box 3110, San Francisco, CA 94158, USA. Tel. +1 415 502 6355. Email: Felix.Feng@ucsf.edu

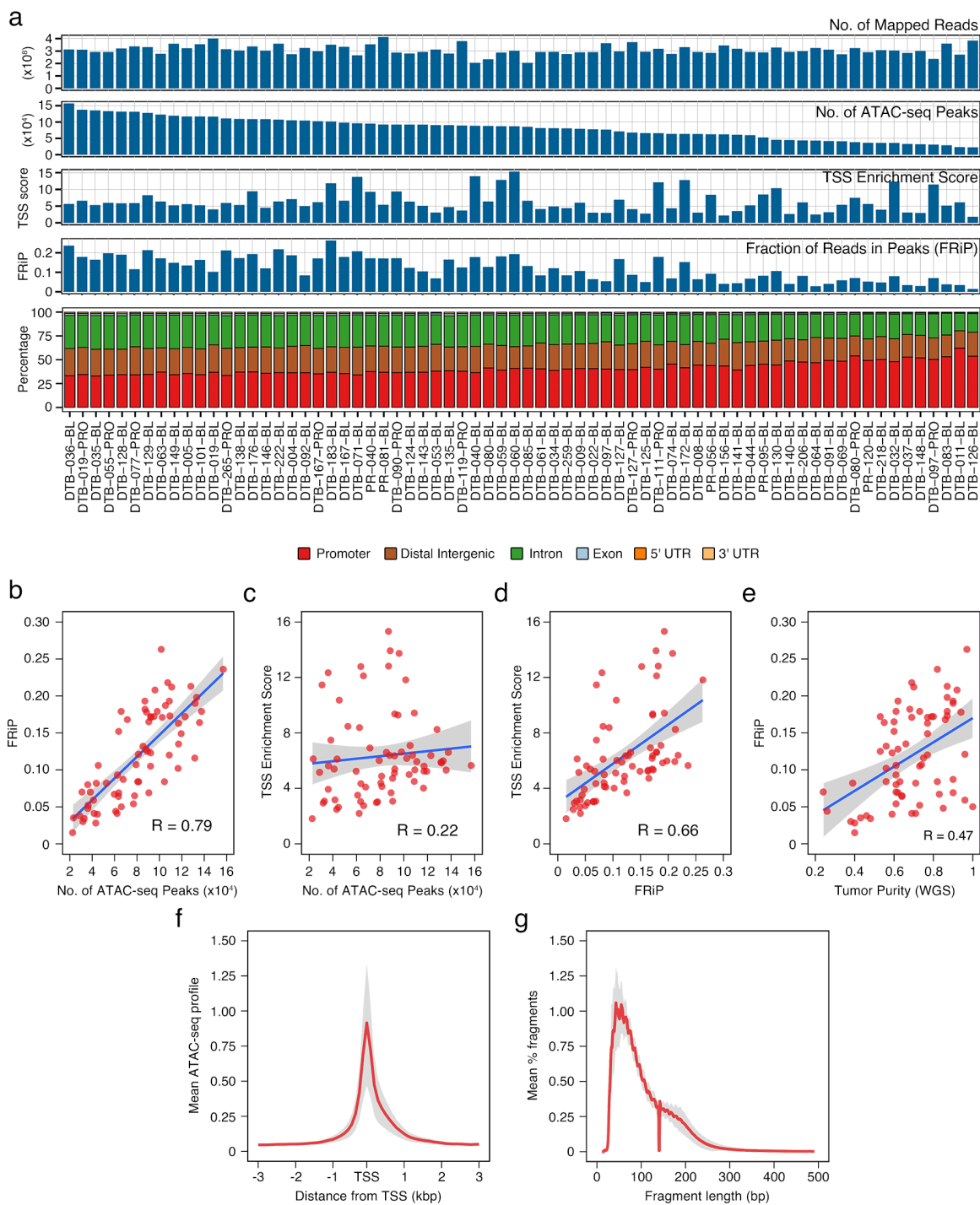
## Supplemental Figures



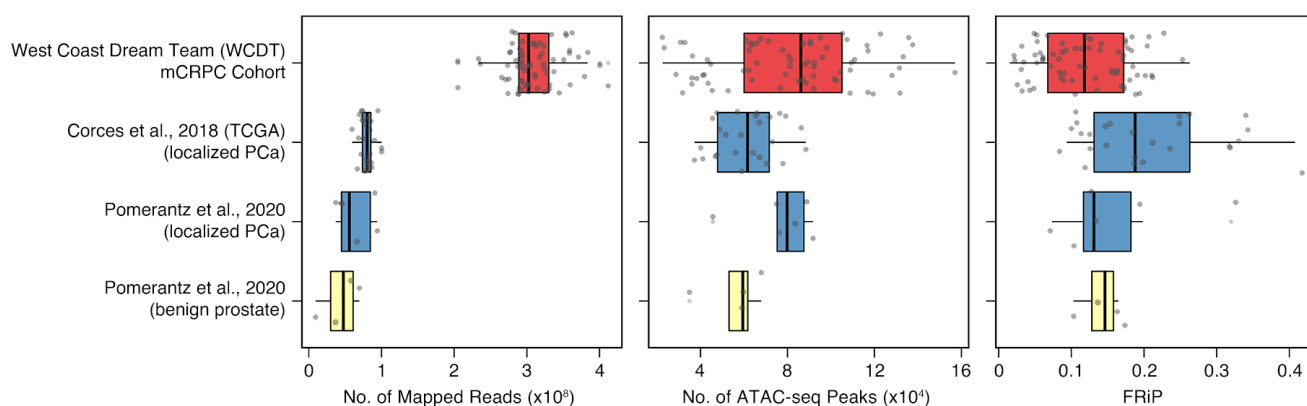
**Supplementary Fig. S1. Overview of metastatic biopsy sites analyzed in this study.** The number of biopsies per metastatic site analyzed with ATAC-seq are shown in parentheses.



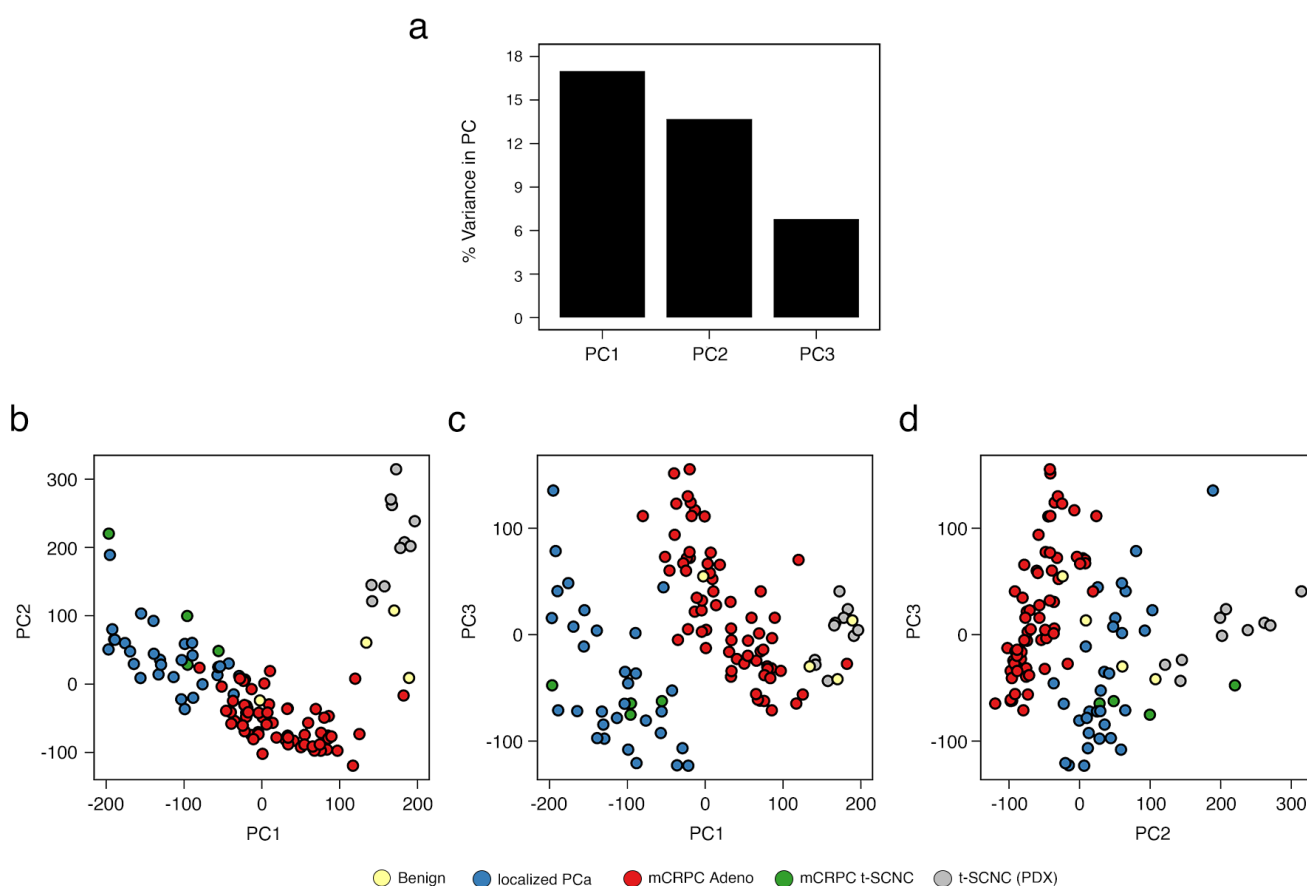
**Supplementary Fig. S2. Schematic diagram illustrating ATAC-seq data processing workflow.**



**Supplementary Fig. S3. ATAC-seq quality control metrics of the mCRPC samples.** (a) Bar plot of the number of mapped reads, number of ATAC-seq peaks detected, Transcription Start Site (TSS) enrichment score, and fraction of reads in peak (FRiP) per sample. The bottom panel represents the percentage of peaks that mapped to promoter, distal intergenic, intron, exon, or UTR region. (b-e) Spearman's correlation of the number of ATAC-seq peaks, FRiP score, TSS enrichment score, and tumor purity. Each dot in the plot represents an individual mCRPC sample. Tumor purity is computed using the matched whole genome sequences (WGS). (f) ATAC-seq signal of all mCRPC samples at TSS $\pm$ 3kb. The solid red line represents the mean signal and the grey shade represents the upper and lower bounds of the ATAC-seq signal. (g) Fragment length distribution of all mCRPC samples. The solid red line represents the mean and the grey shade represents the upper and lower bounds of the distribution.

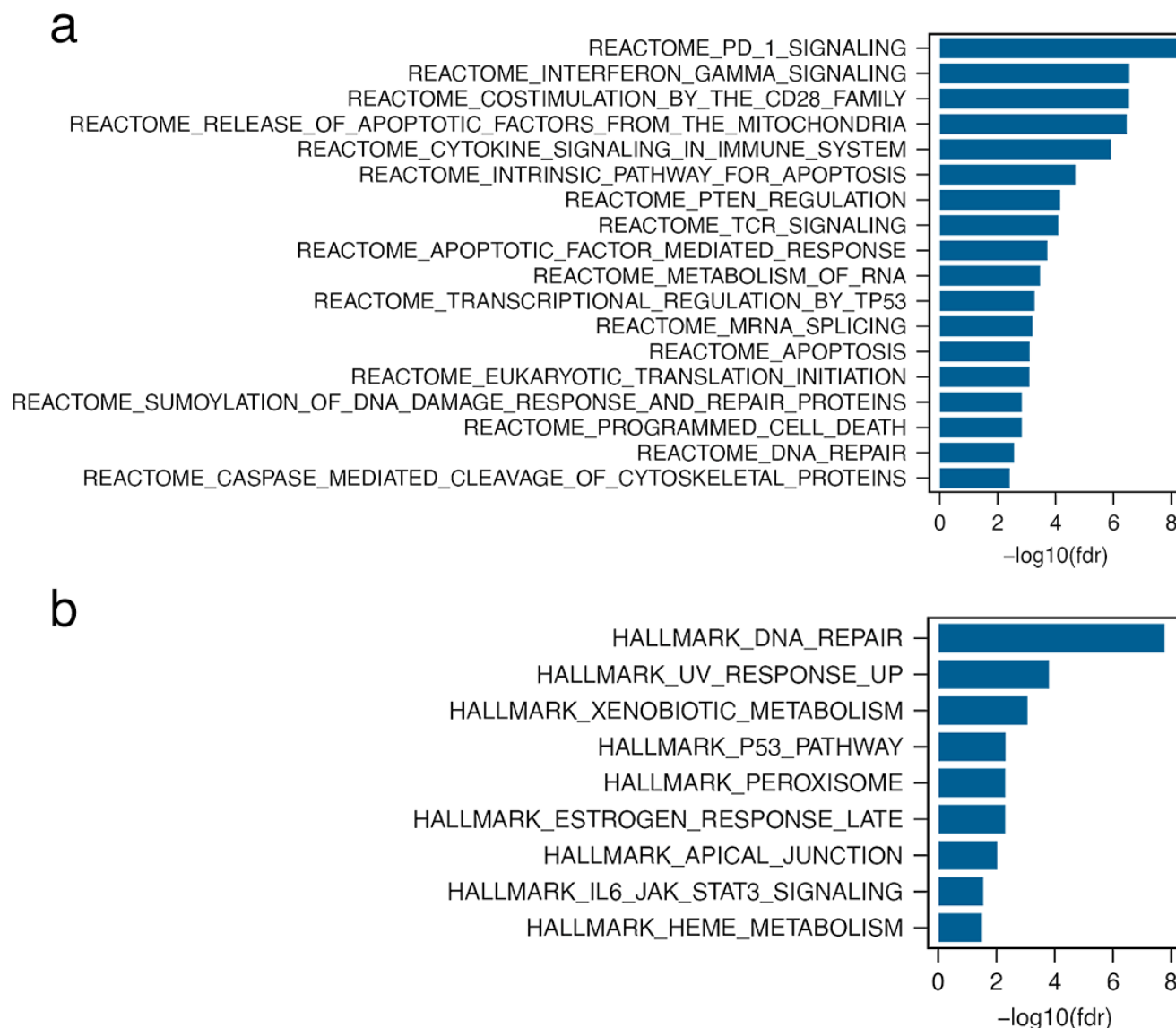


**Supplementary Fig. S4. Comparison of ATAC-seq quality of mCRPC samples with publicly available datasets.** Comparison of the number of mapped sequencing reads, the number of ATAC-seq peaks, and FRiP score between the West Coast Dream Team (WCDT) mCRPC cohort (this study), Corces et al. (Corces et al. 2018), and Pomerantz et al. (Pomerantz et al. 2020) cohorts. Note: for a fair comparison, we have only included ATAC-seq profiles obtained from tissue samples (Cell lines and PDX samples are not included). The ENCODE guideline (<https://www.encodeproject.org/atac-seq>) recommends using ATAC-seq samples with FRiP scores greater than 0.2. However, it's important to note that these recommendations were primarily derived from experiments conducted in cell lines and may not directly translate to ATAC-seq experiments conducted in tissue samples. For example, the TCGA pan-cancer ATAC-seq study (Corces et al. 2018) used several samples with FRiP scores below this threshold. In fact, 57.7% (15 out of 26) of the prostate cancer tissue samples in the TCGA study had FRiP scores below 0.2. The study by Pomerantz et al. (Pomerantz et al. 2020) reported 5 out of 6 prostate cancer tissue samples and all 4 benign prostate tissue samples with FRiP scores below 0.2. It is possible that different FRiP thresholds may be necessary to assess the quality of tissue samples.



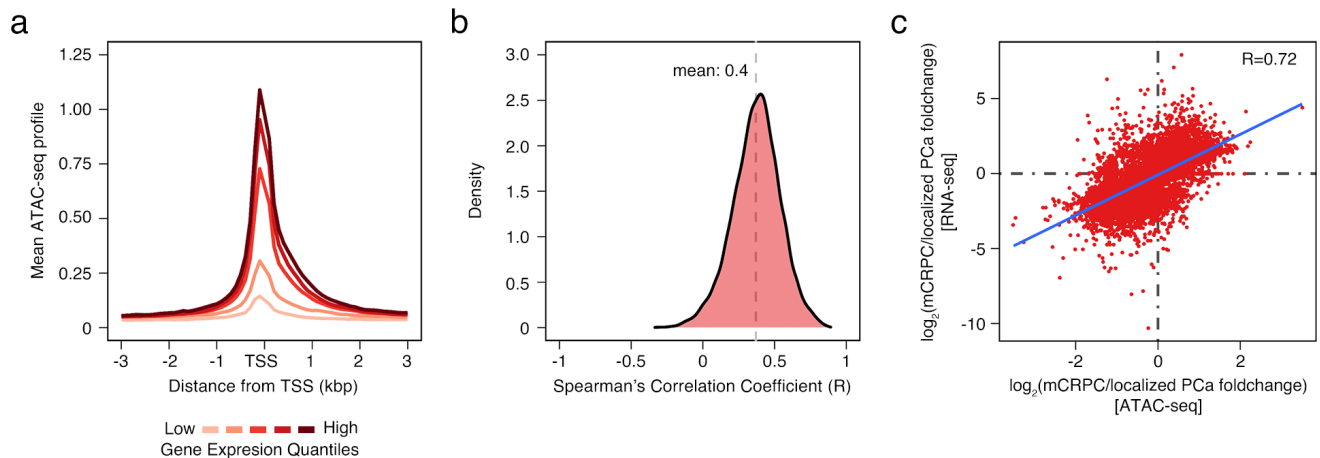
**Supplementary Fig. S5. PCA of the ATAC-seq profiles comparing different stages of prostate cancer.** (a) Variance captured in the principal components PC1, PC2, and PC3. (b-d) PCA of the ATAC-seq profiles comparing benign prostate, localized prostate cancer (PCa), mCRPC Adeno, and mCRPC t-SCNC/NEPC. The normalized read counts of these consensus-accessible regions were used for the PCA analysis. Each dot in the plot represents an individual sample.



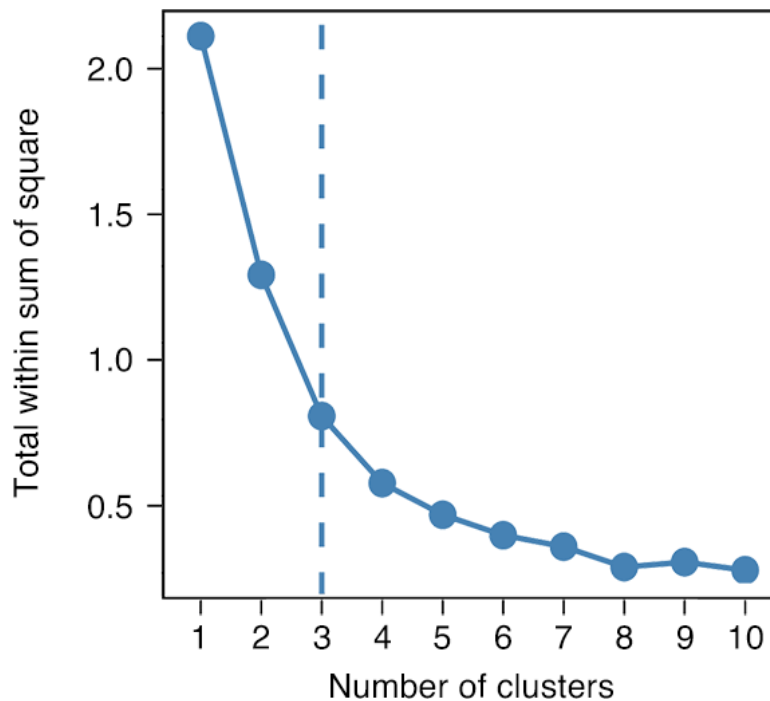


**Supplementary Fig. S6. Enrichment of accessible chromatin region in malignant prostate cancer.**

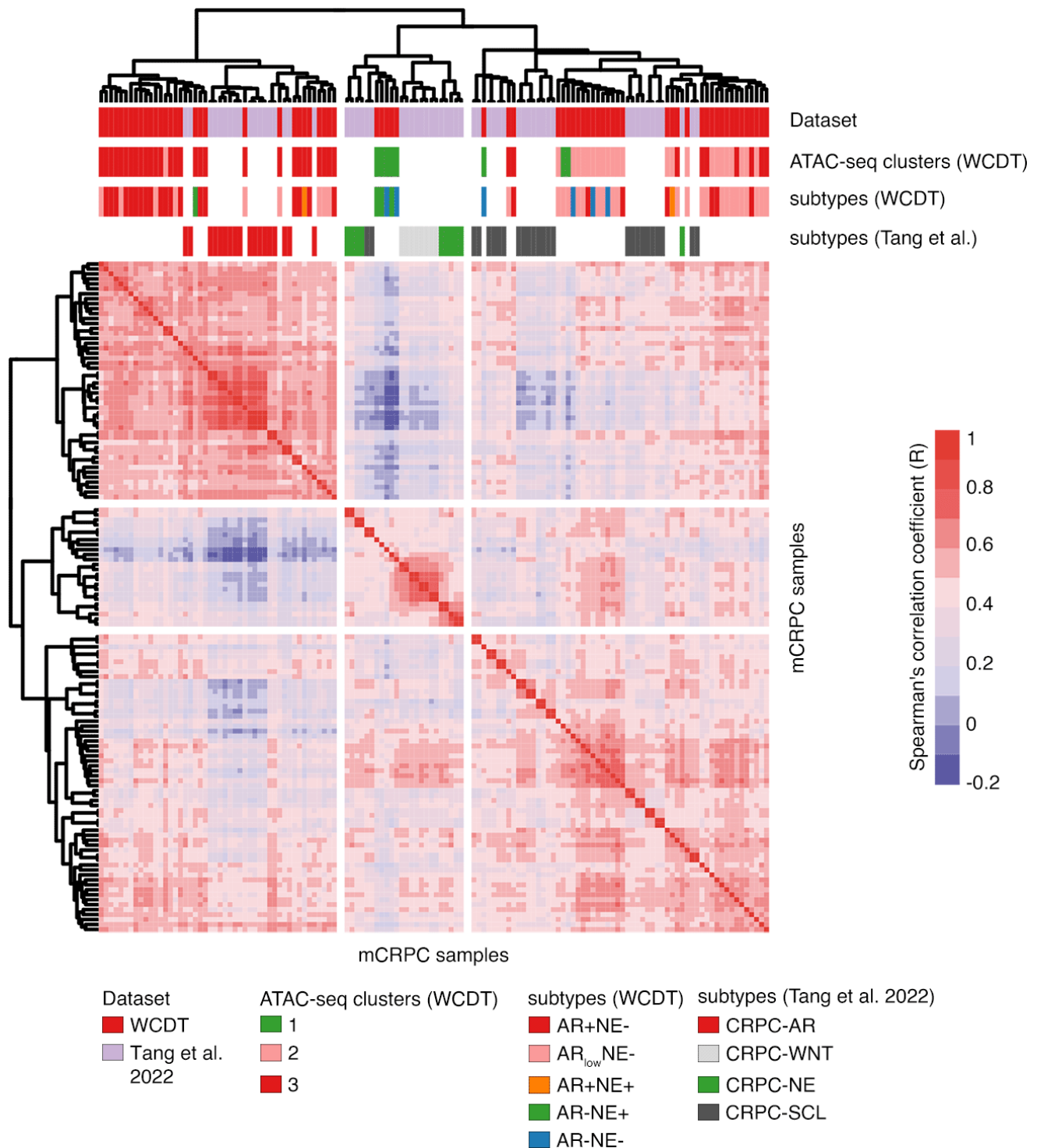
Enrichment of accessible chromatin regions common between localized PCa, mCRPC (adeno), and t-SCNC/NEPC but not accessible in benign prostate cancer tested against (a) Reactome pathways and (b) Hallmark pathways. The enrichment analysis was carried out using the rGREAT R-package.



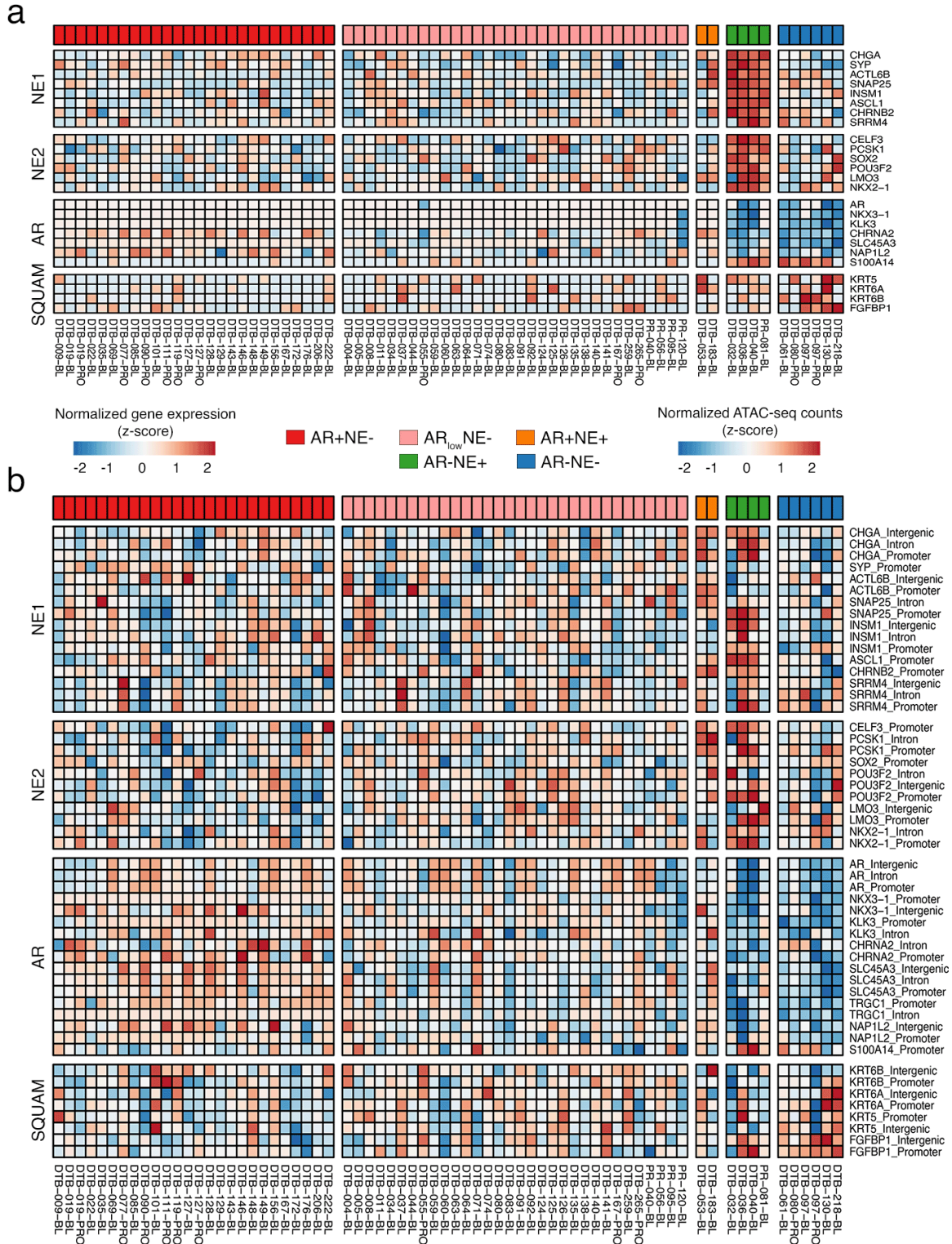
**Supplementary Fig. S7. Correlation of ATAC-seq peak accessibility and corresponding RNA-seq gene expression levels.** (a) ATAC-seq signal profile segregated by gene expression quantiles measured at  $\text{TSS} \pm 3\text{kb}$  measured in the sample DTB-063-BL. (b) Spearman's correlation of gene-promoter accessibility (i.e. normalized ATAC-seq read counts) with corresponding RNA-seq gene expression measured across 70 mCRPC samples. (c) Correlation of the differentially expressed genes between mCRPC and localized PCa and their nearby ATAC-seq peaks. Each dot in the plot represents a gene. About 85% of differentially expressed genes between mCRPC and localized PCa were positively correlated (Spearman's correlation coefficient  $R=0.72$ ) with their nearby ATAC-seq peaks.



**Supplementary Fig. S8. Estimating ATAC-seq clusters of mCRPC samples.** Estimation of the optimum number of ATAC-seq clusters using the elbow method.

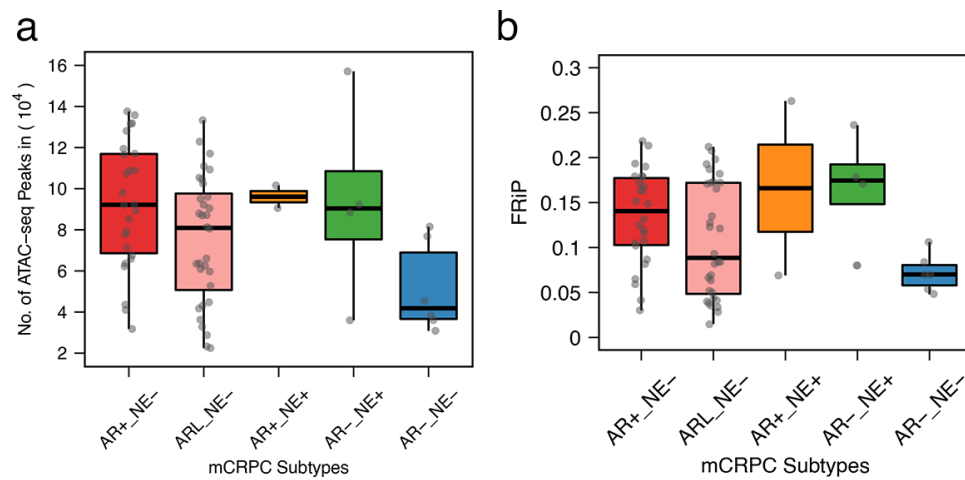


**Supplementary Fig. S9. ATAC-seq unsupervised clusters of mCRPC samples.** Pairwise Spearman's correlation heatmap of ATAC-seq profiles of samples from both the West Coast Dream Team (WCDT) cohort (this study) and those from Tang et al. (Tang et al. 2022). The two datasets were combined and corrected for potential batch effects using the 'ComBat' function from the 'sva' R-package. The correlation is based on the normalized number of reads of the top 1% variable peaks across all samples.



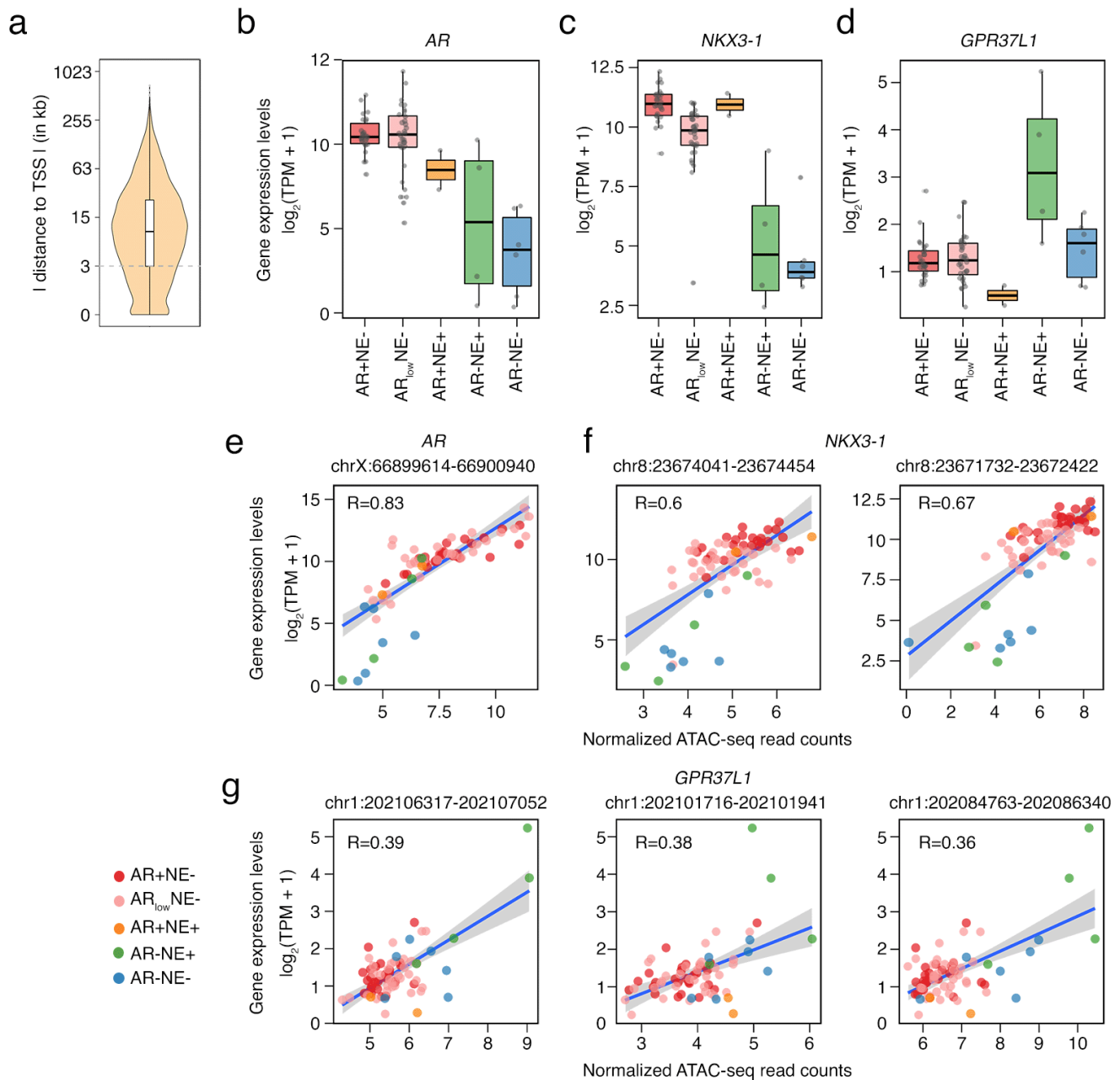
**Supplementary Fig. S10. mCRPC transcriptional subtypes classification based on Labrecque et al.**

**genelist.** (a) RNA-seq gene expression profile and (b) ATAC-seq chromatin accessibility profile of mCRPC samples based on the genelist from Labrecque et al. (Labrecque et al. 2019). NE: Neuroendocrine, AR: Androgen Receptor, SQUAM: Squamous

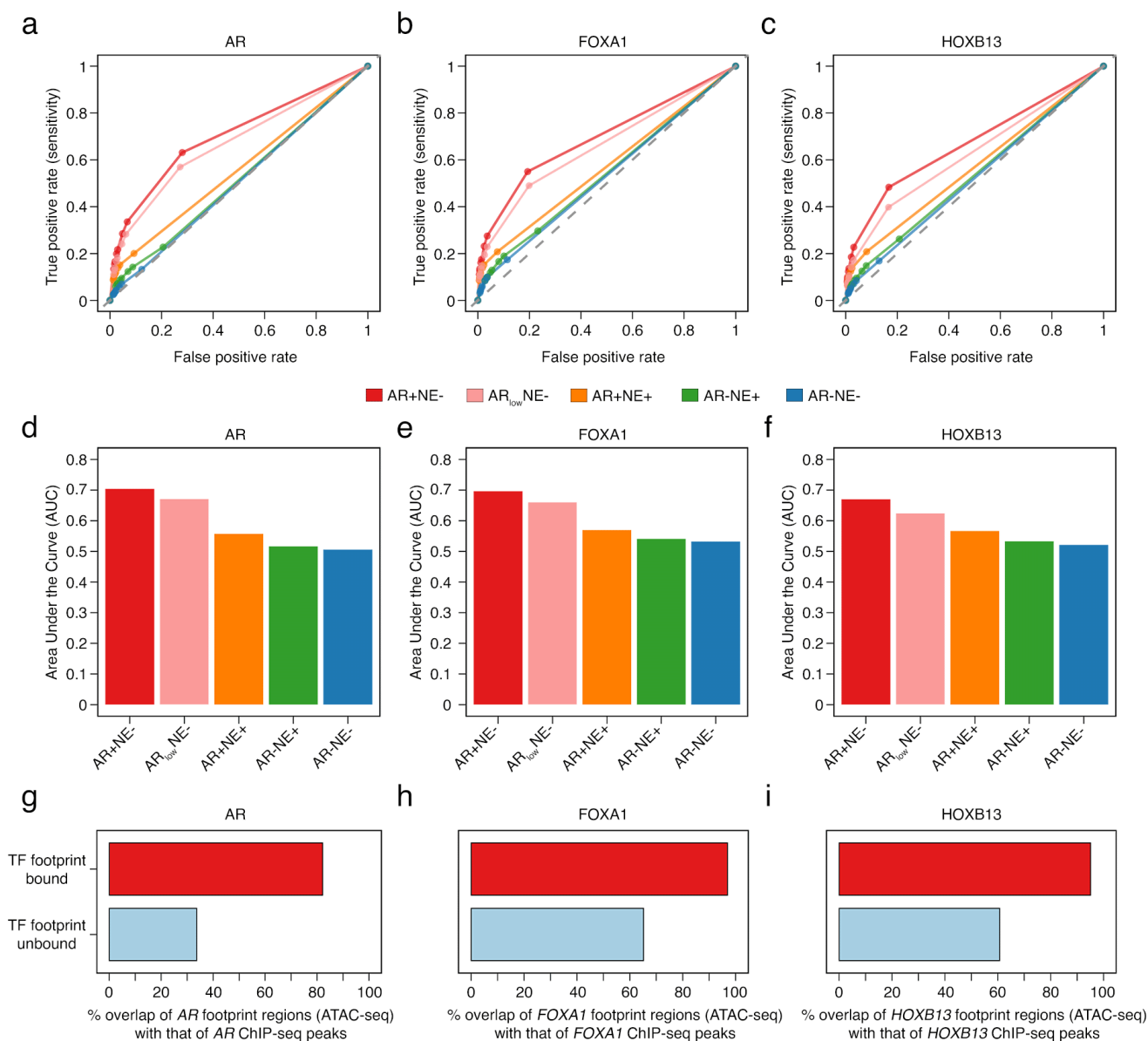


**Supplementary Fig. S11. Association of ATAC-seq peaks quality metrics with mCRPC transcriptional subtypes.** (a) Box plot of the number of ATAC-seq peaks and (b) FRiP score of mCRPC grouped by mCRPC transcriptional subtypes.

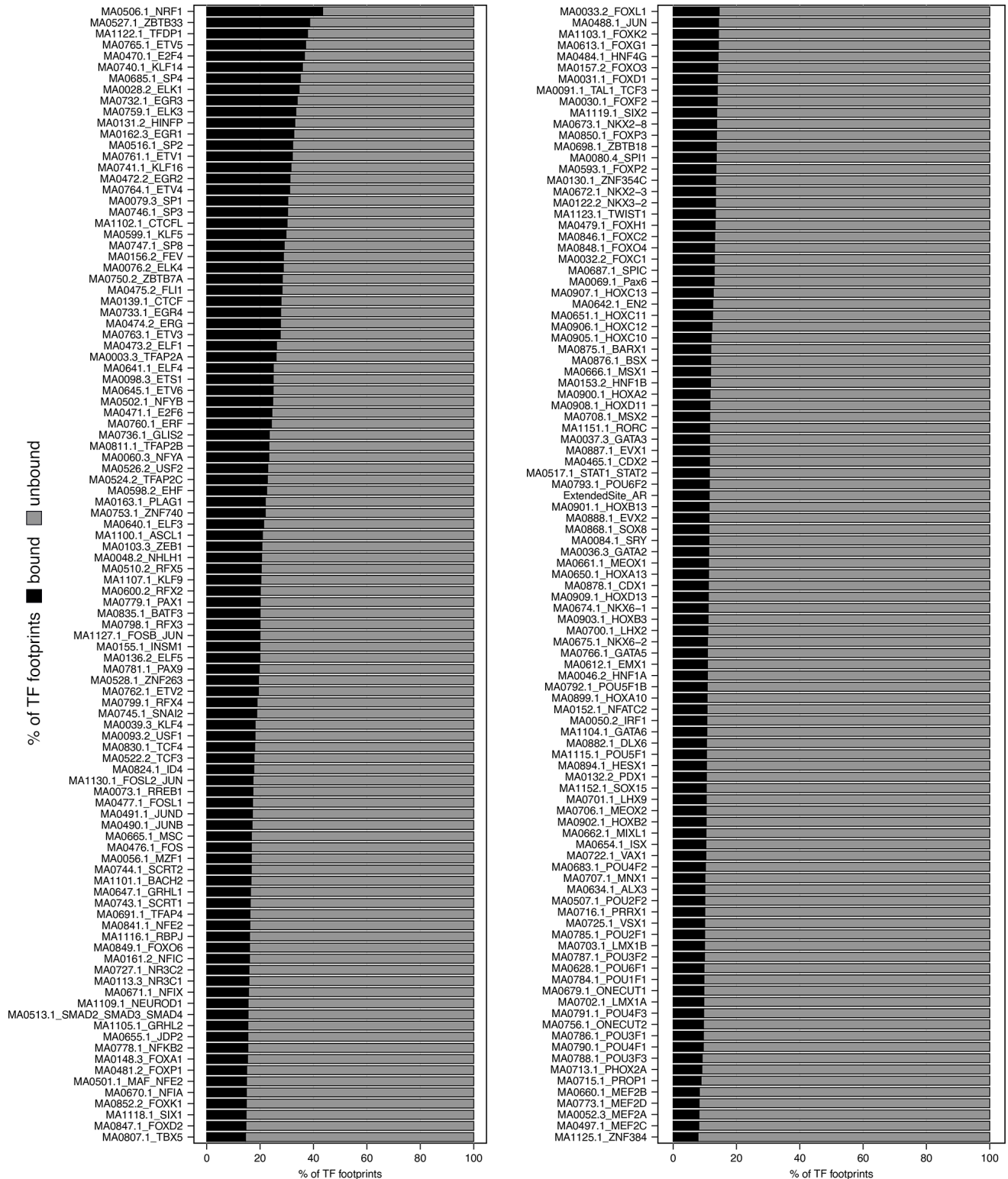




**Supplementary Fig. S12. Gene expression levels between mCRPC transcriptional subtypes.** (a) Violin boxplot illustrating the distribution of the absolute distance of the chromatin variants between mCRPC transcriptional subtypes to the nearest gene TSS. (b-d) Boxplot of (b) *AR*, (c) *NKX3-1*, and (d) *GPR37L1* gene expression levels between the mCRPC transcriptional subtypes. (e-g) Correlation of RNA-seq gene expression levels and its corresponding normalized ATAC-seq read counts of potential enhancer in the distal intergenic region. Each dot represents a mCRPC sample and its color designates a corresponding mCRPC transcriptional subtype. The Spearman's correlation coefficient ( $R$ ) between the ATAC-seq and RNA-seq is indicated in the plot.

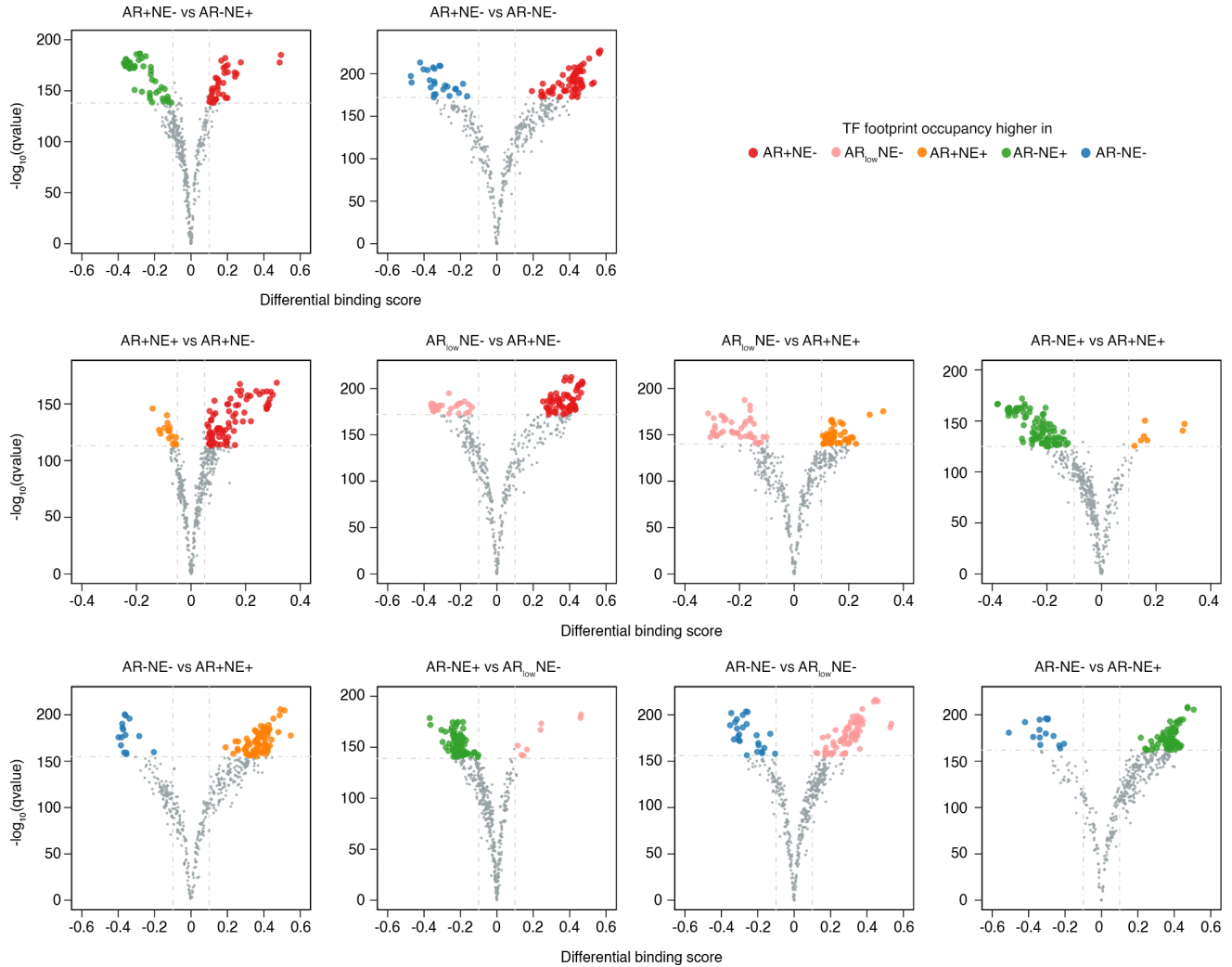


**Supplementary Fig. S13. Evaluation of the reliability of TF-footprint sites.** (a-c) Receiver operating characteristic (ROC) curve was generated to assess the consistency between the predicted TF footprints identified by TOBIAS using ATAC-seq and the experimentally identified TF-binding sites using ChIP-seq. Here, TF-footprints from our mCRPC ATAC-seq cohort were compared against ChIP-seq (a) *AR*, (b) *FOXA1*, and (c) *HOXB13* data of mCRPC PDX samples from Pomerantz et al. (Pomerantz et al. 2020). The mCRPC PDX samples in the Pomerantz et al. study represent the AR+NE- subtype. Each colored line represents the comparison using the respective mCRPC transcriptional subtype. AR+NE- subtype achieved the highest area under the ROC curve (AUC) followed by AR<sub>low</sub>NE- subtype. The rest of the three mCRPC subtypes AR+NE+, AR-NE+, and AR-NE- achieved very low AUC because the ChIP-seq data from mCRPC resembles the AR+ subtype. (d-f) Area under the curve (AUC) of the TF footprints to ChIP-seq peaks comparison for each mCRPC subtype. (g-i) Percentage of overlap of TF footprint sites predicted using ATAC-seq (bound p-value threshold = 0.001) with that of respective ChIP-seq peak sites (g) *AR*, (h) *FOXA1*, and (i) *HOXB13* of mCRPC PDX samples from the Pomerantz et al. study. The TF footprint sites are grouped by bound and unbound sites.

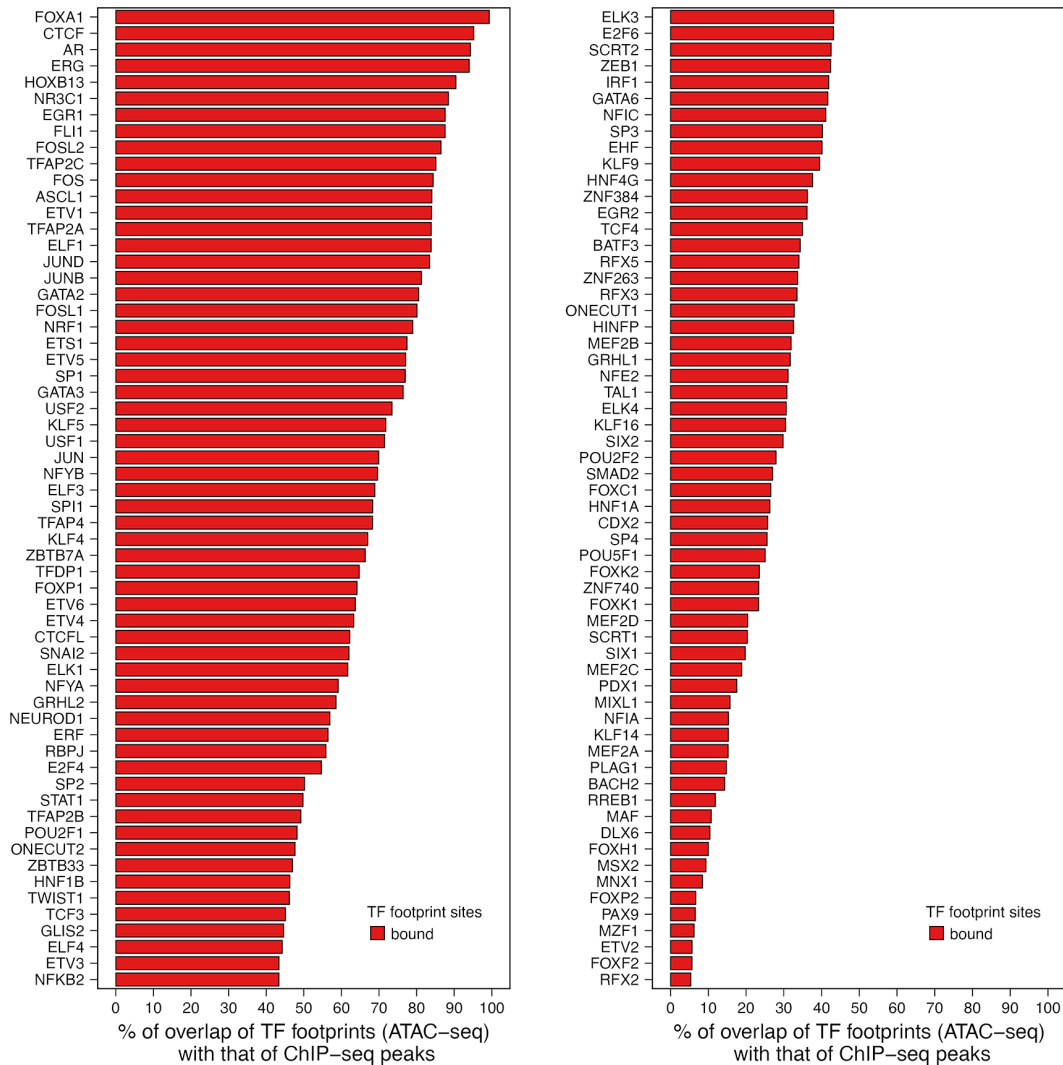


**Supplementary Fig. S14. Percentage of TF footprint sites classified as bound and unbound.** TOBIAS categorizes every predicted TF binding site (for each TF motif) into bound and unbound states based on a score threshold per subtype compared. The threshold was set at the level of significance (bound p-value=0.001) of a normal distribution fit to the background distribution of scores. Note: Only 203 mCRPC-associated TF predicted from our TF footprint analysis are shown in the figure due to limitations in figure space.

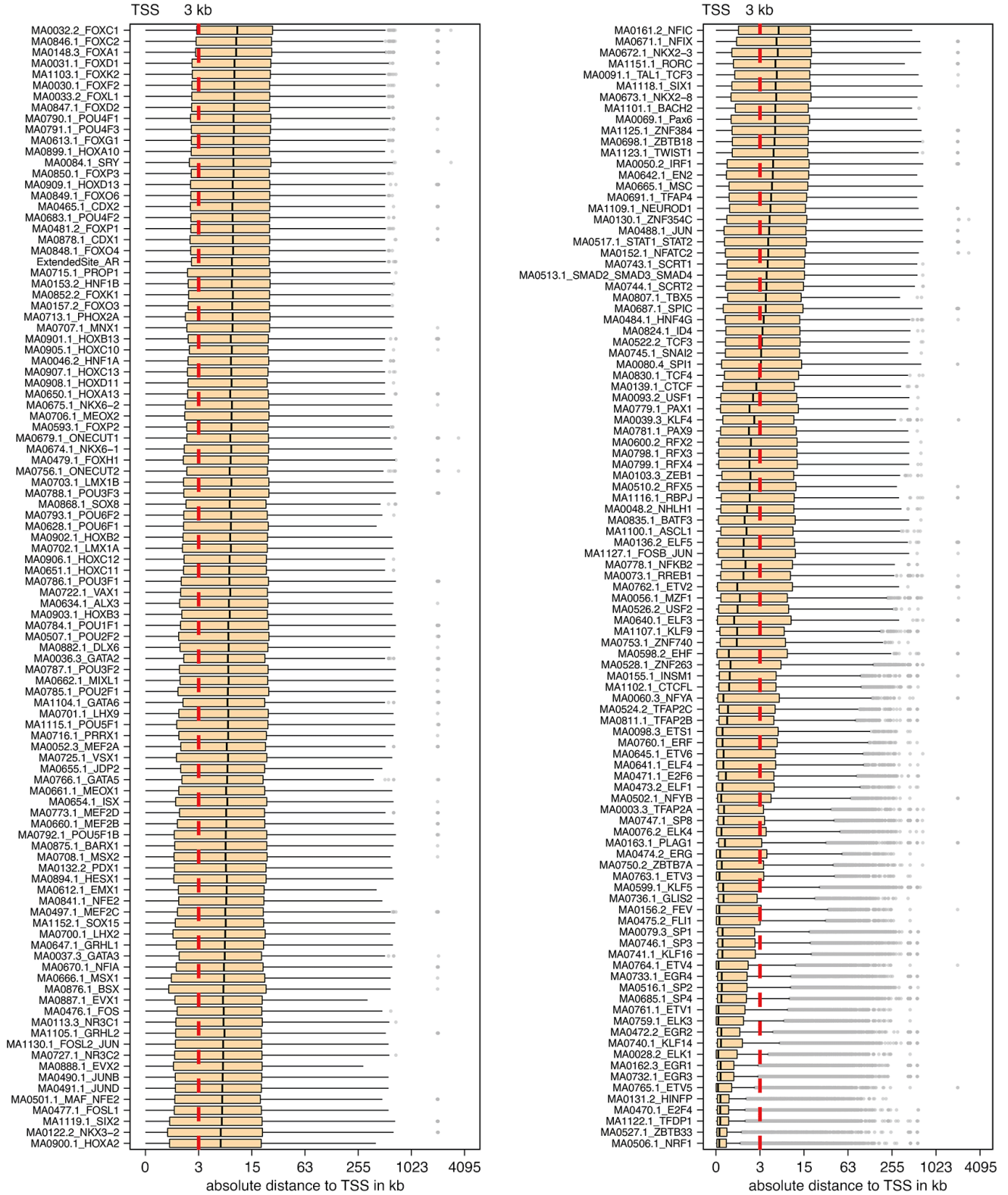




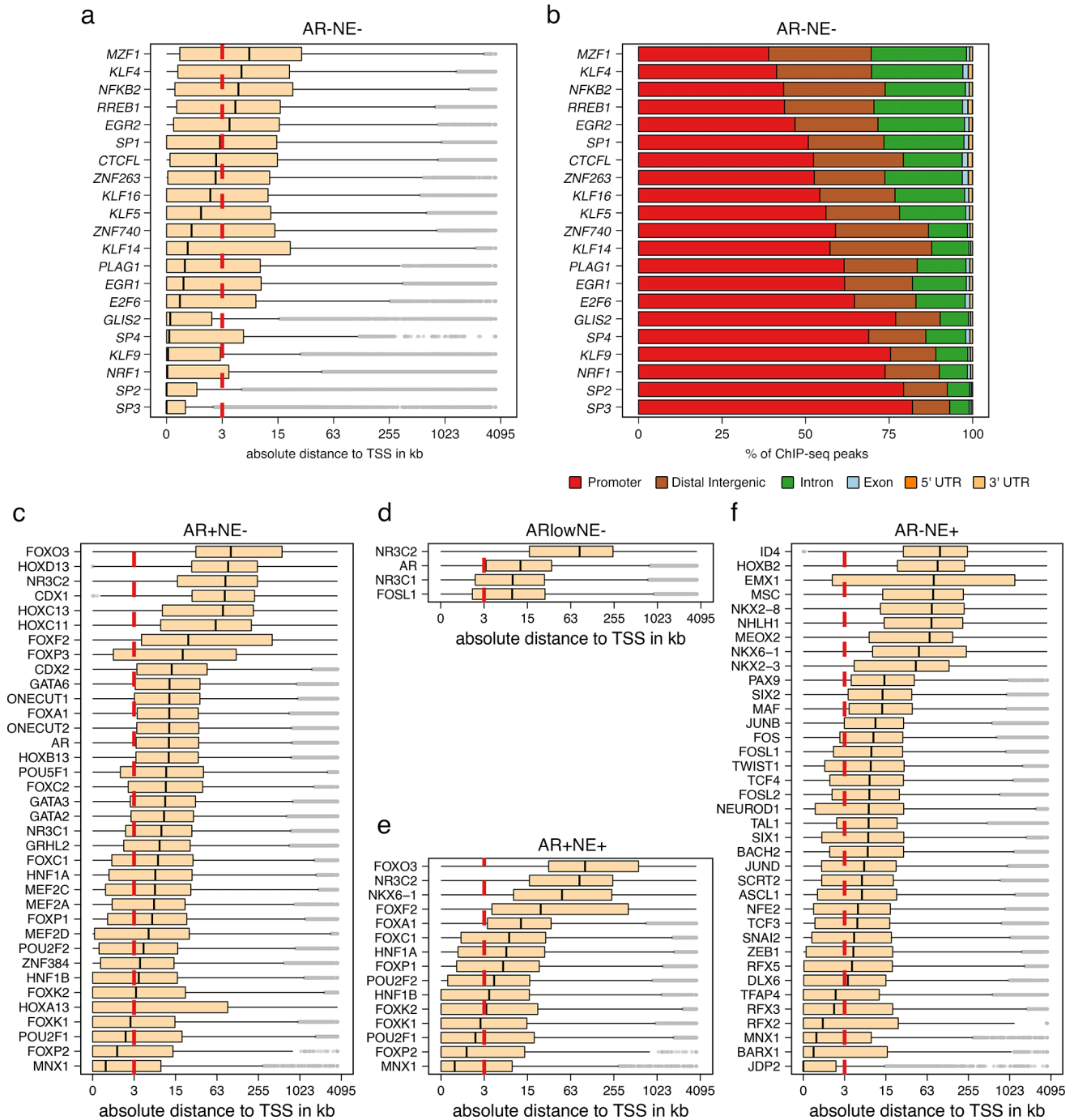
**Supplementary Fig. S15. Differential TF footprint occupancy between mCRPC transcriptional subtypes.** Differential TF footprint occupancy analysis comparing the mCRPC transcriptional subtypes. The colored dots indicate a significantly differentially bound TF motif. Note: Data available as Supplementary Table S3. The plots comparing AR+NE- vs AR-NE+ and AR+NE- vs AR-NE- are presented in detail in Figure 4c-d.



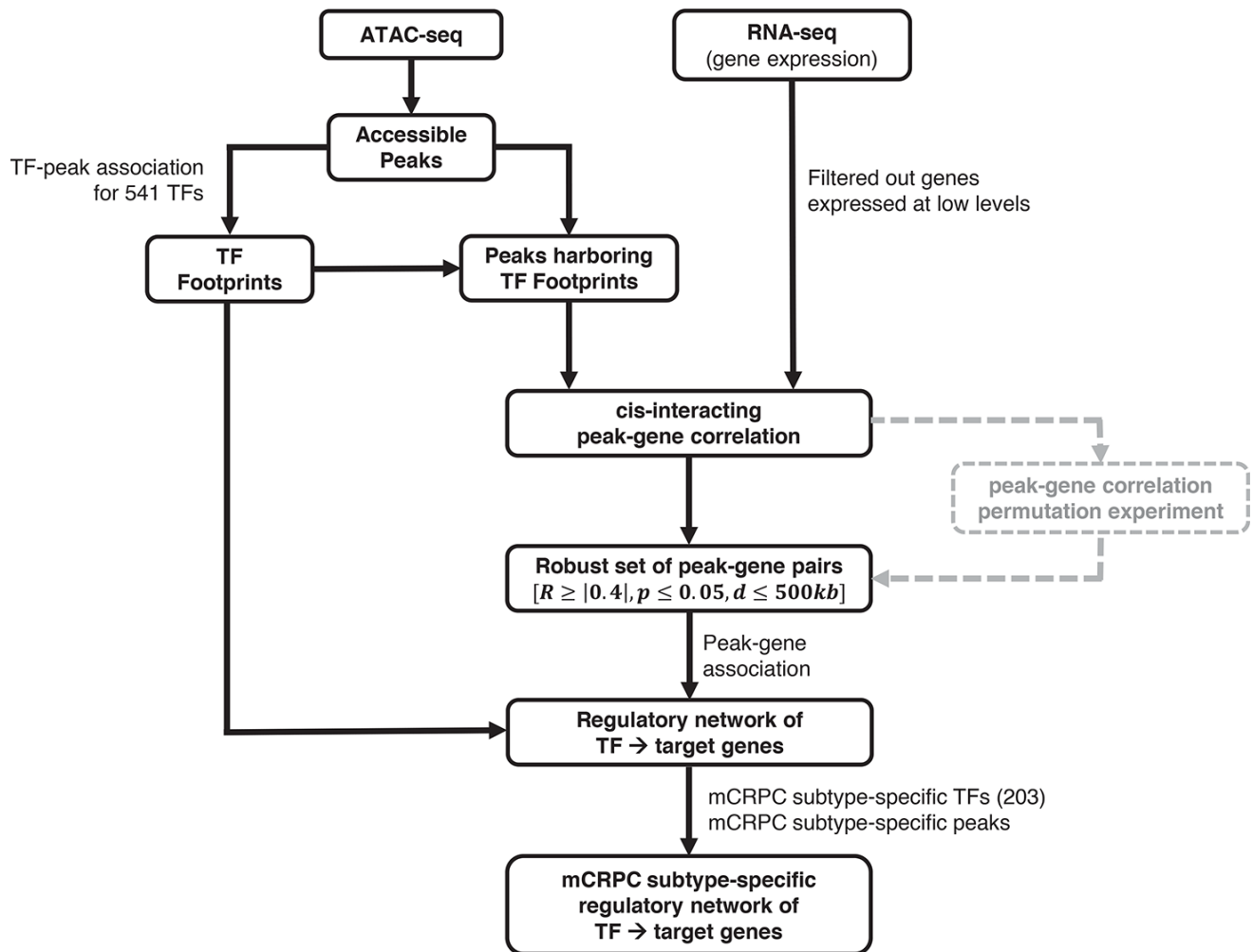
**Supplementary Fig. S16. Correlation of ATAC-seq predicted TF footprint sites with ChIP-seq peaks.** The percentage of overlap between ATAC-seq predicted TF footprint sites and those predicted by ChIP-seq from publicly available datasets in the ChIP-Atlas (Oki et al. 2018) database. The percent overlap in the figure above is calculated out of total bound TF-footprint sites. Among the 203 mCRPC-associated TFs predicted in this study, ChIP-seq profiles were available for 157 TFs in the ChIP-Atlas database, which compiles ChIP-seq profiles from diverse datasets obtained from various tissue sites or cell lines, including prostate and prostate cancer. We identified 120 TFs where more than 5% of TF footprints coincided with regions identified by ChIP-seq peaks. The comparison of TF footprint sites for these 120 TFs with corresponding ChIP-seq datasets is shown in the figure above. The remaining 37 TFs showed minimal overlap in TF footprints with their corresponding ChIP-seq datasets, mainly due to disparities in tissue-site matching, and were thus excluded from the analysis.



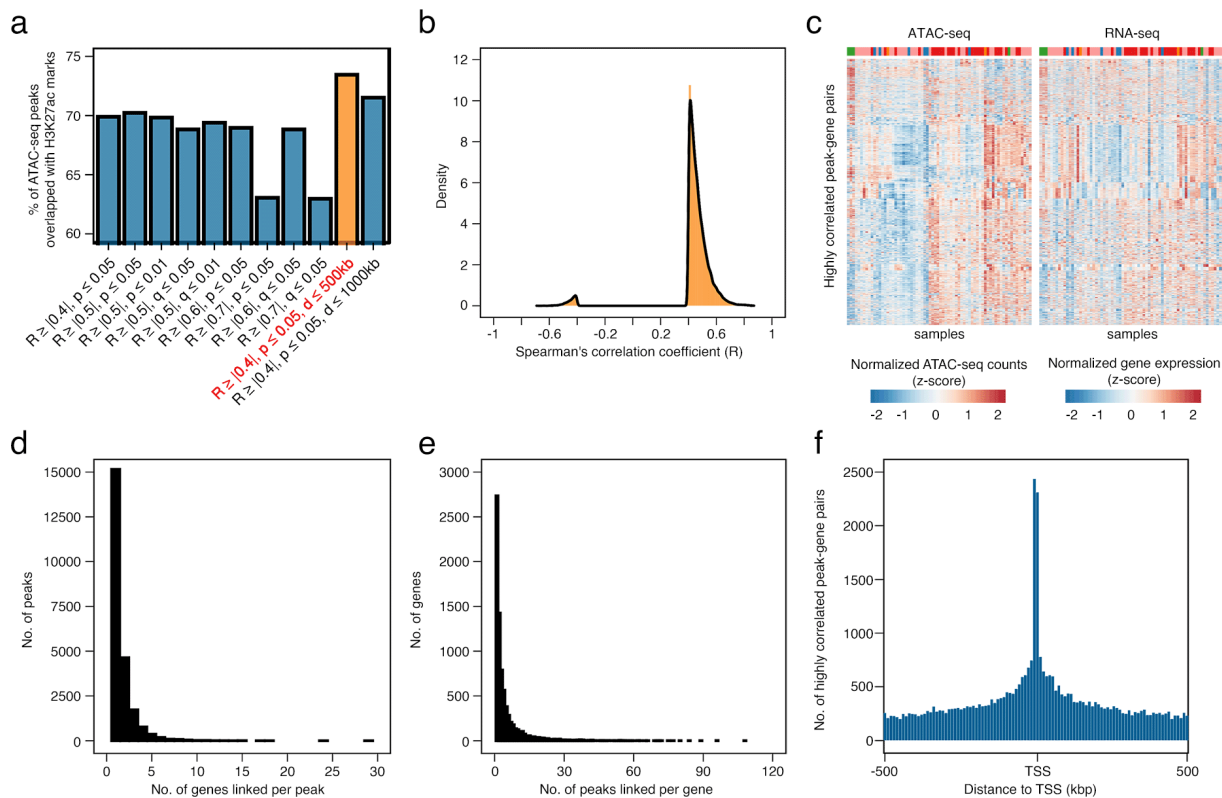
**Supplementary Fig. S17. Distribution of TF footprints distance to the TSS of the nearest gene.** Boxplot illustrating the distribution of the absolute distance of the bound TF footprints to the nearest gene TSS. The vertical dashed line indicates 3kb mark from the TSS (i.e. gene promoter region).



**Supplementary Fig. S18. Distribution of ChIP-seq peaks of mCRPC subtype associated TF.** (a) Boxplot illustrating the distribution of the absolute distance of the TF binding sites as predicted by ChIP-seq to the nearest gene TSS. The TFs are associated with AR-NE- subtype. The vertical dashed line indicates 3kb mark from the TSS (i.e. gene promoter region). (b) The percentage of ChIP-seq peaks that mapped to promoter, distal intergenic, intron, exon, or UTR region. The ChIP-seq peaks used for these analyses were publicly available and downloaded from the ChIP-Atlas ([Oki et al. 2018](#)) database. (c-f) Boxplot illustrating the distribution of the absolute distance of the TF binding sites as predicted by ChIP-seq to the nearest gene TSS. The TFs are associated with (c) AR+NE-, (d) ARlowNE-, (e) AR+NE+, and (f) AR-NE+ subtype.

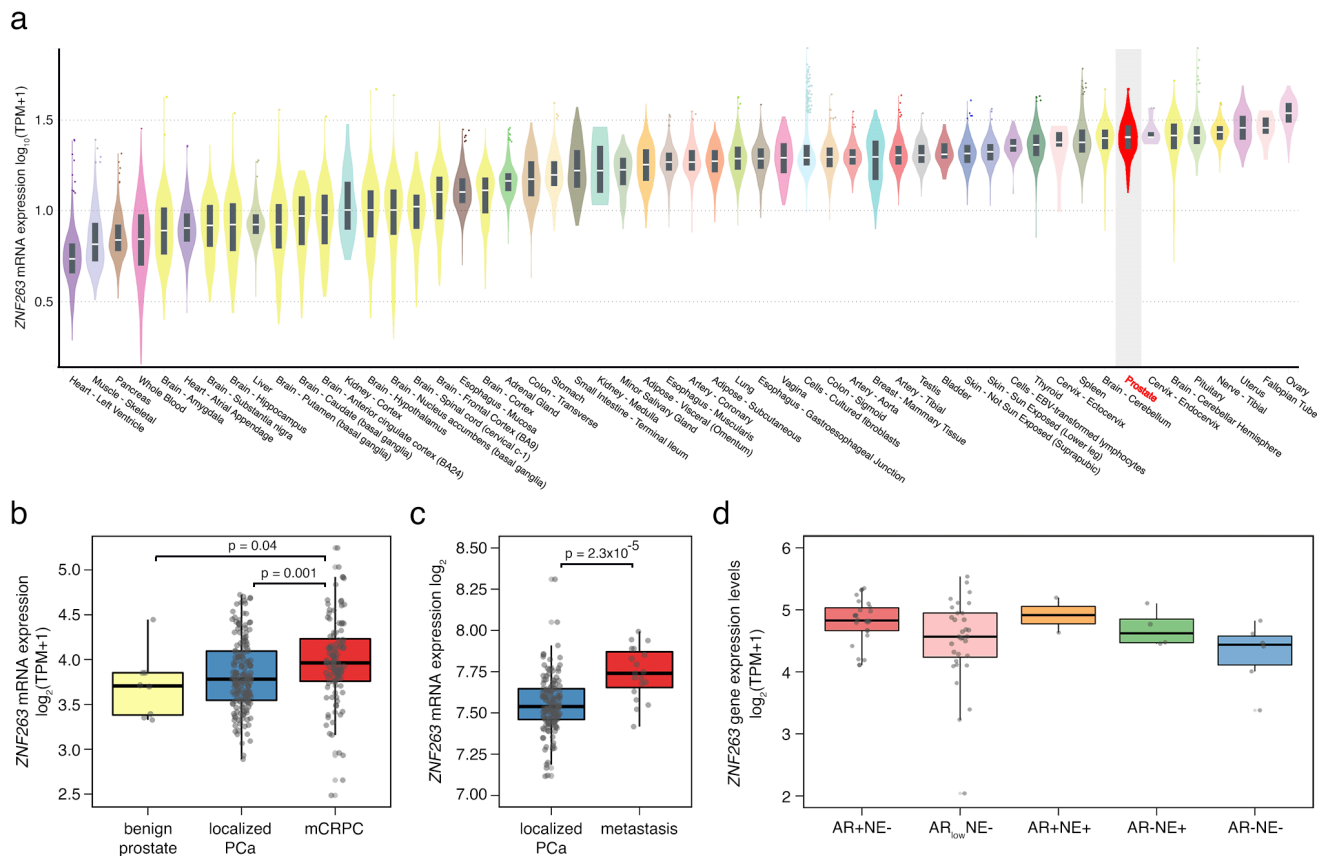


**Supplementary Fig. S19.** Schematic workflow diagram illustrating the construction of TF-target gene regulatory network.



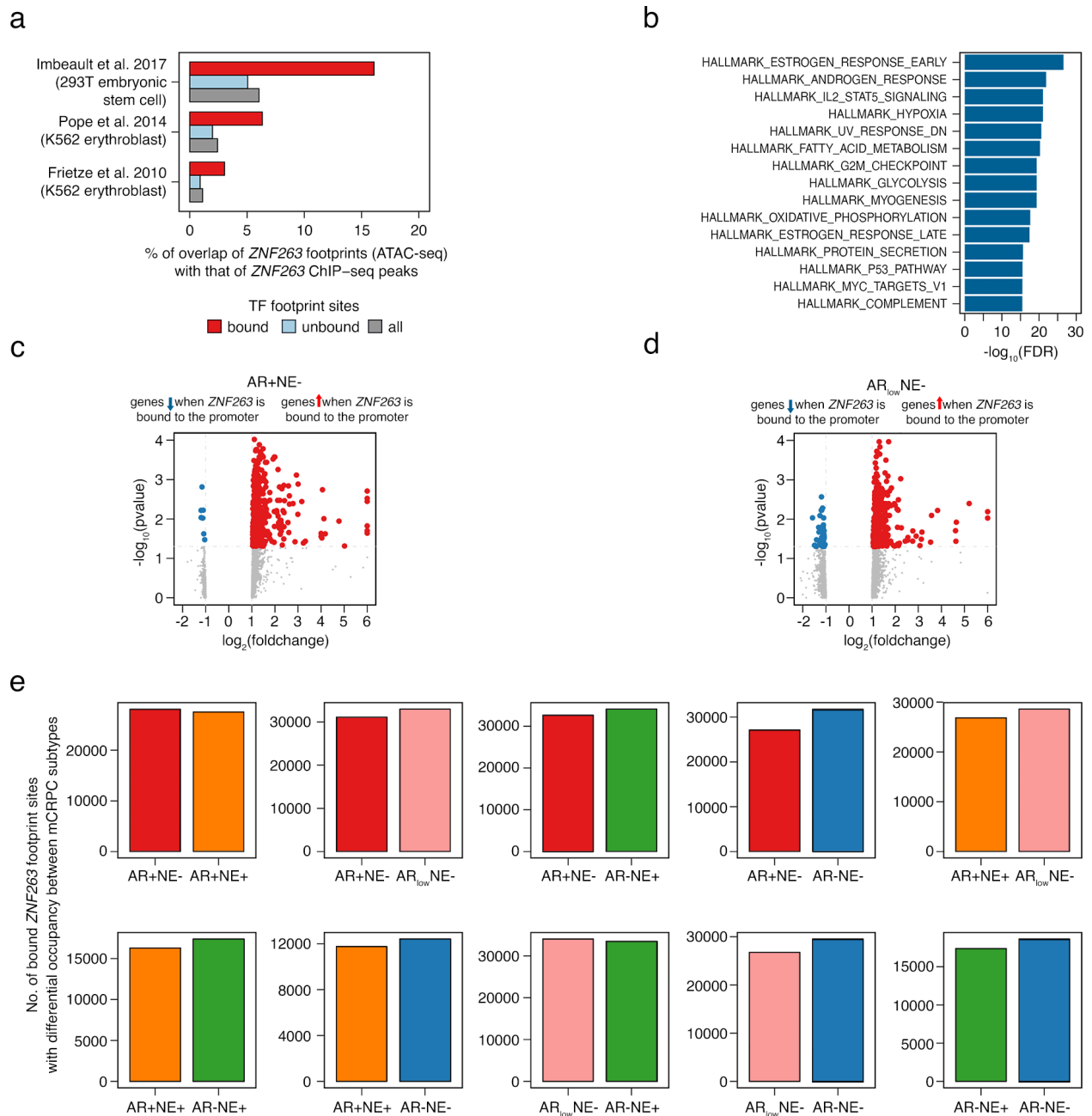
### Supplementary Fig. S20. Prediction of ATAC-seq peaks potentially regulating gene expression. (a)

Selection of optimum parameters to retain the most robust set of correlated or anti-correlated peaks-gene pairs. The peak-gene pairs were filtered using different parameters such as Spearman's correlation coefficient (R), p-value (p), q-value (q), and distance of the peak to TSS (d). The plot indicates the percentage of peaks overlapped with H3K27ac ChIP-seq marks. (b) Distribution of Spearman's correlation coefficient (R) of the robust set of peak-gene pairs after filtering using the parameters:  $R \geq |0.4|$ ,  $p \leq 0.05$ , and  $d \leq 500kb$  (c) Heatmap of ATAC-seq and RNA-seq profiles of highly correlated peak-gene pairs in our mCRPC cohort. Each row of the heatmap represents an ATAC-seq peak and its corresponding correlated gene. (d) Histogram distribution of the number of genes linked per ATAC-seq peak. (e) Histogram distribution of the number of ATAC-seq peaks linked per gene. (f) The plot illustrates the number of peak-gene pairs predicted as a function of distance from the TSS of the paired gene.



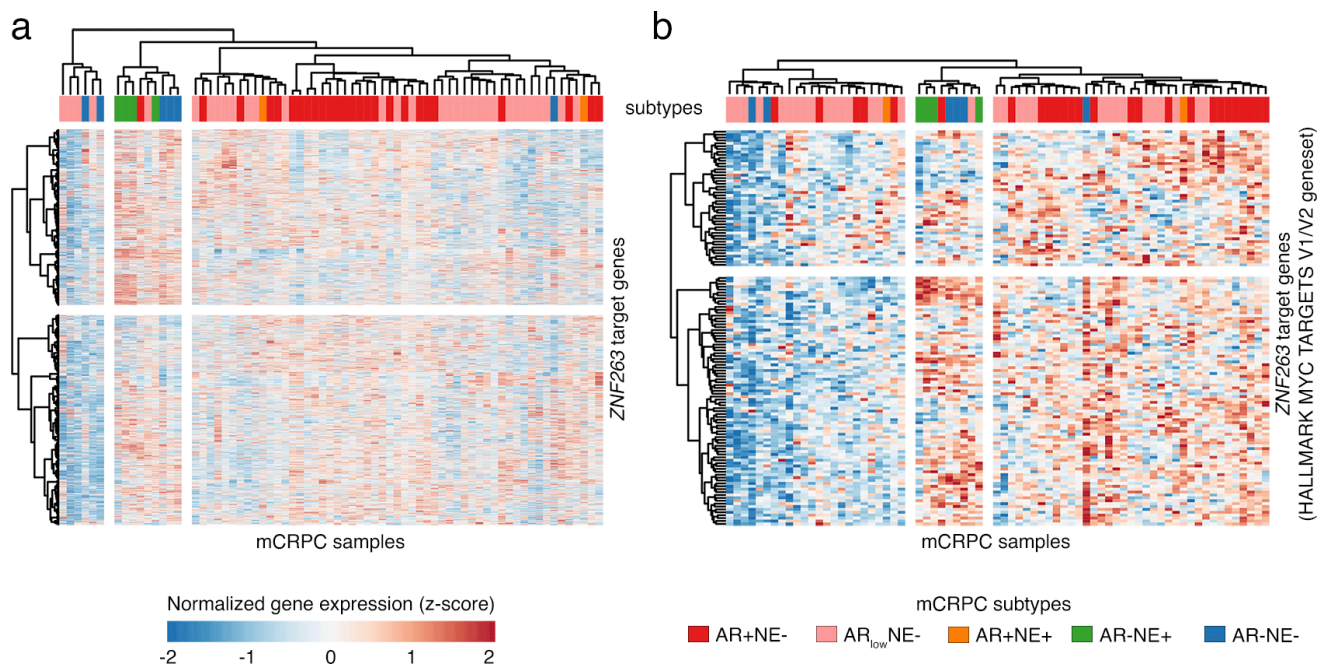
**Supplementary Fig. S21. *ZNF263* mRNA expression in prostate tissues.** (a) Violin plots of *ZNF263* mRNA expression level distributions in non-diseased tissues (including prostate) from the GTEx project ([Consortium 2013](#)). (b) Box plot comparing the distribution of *ZNF263* mRNA expression in benign prostate tissue, localized PCa, and mCRPC tissue samples. The benign prostate tissues are obtained from the PAIR cohort ([Pinskaya et al. 2019](#)), the localized PCa tissues are obtained from the PAIR and CPGC ([Chen et al. 2019](#)) cohorts, and the mCRPC samples are from the WCDT cohort. (c) Box plot comparing distribution of *ZNF263* mRNA expression in localized PCa and metastatic tissue samples from ([Taylor et al. 2010](#)). (d) Box plot of *ZNF263* mRNA expression level distributions between mCRPC subtypes in WCDT cohort.



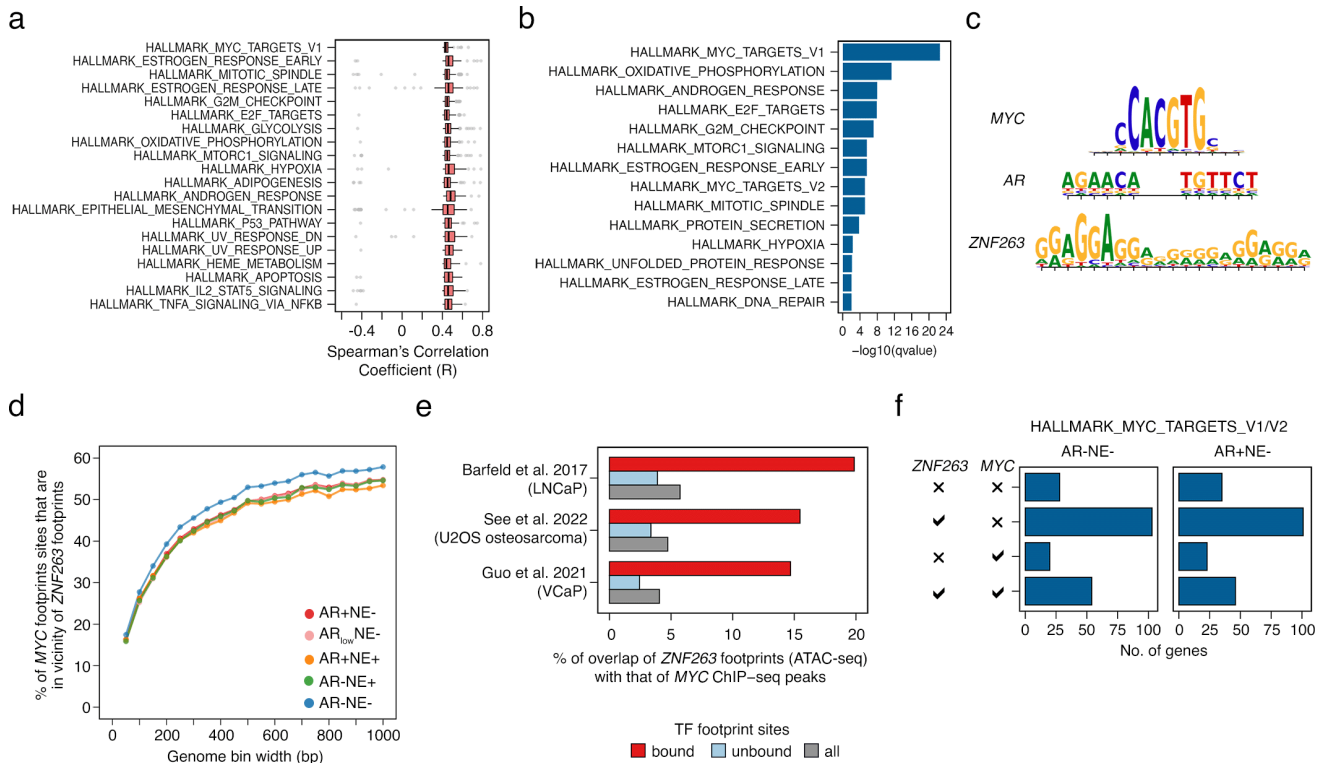


**Supplementary Fig. S22. The effects of *ZNF263* binding on its downstream target genes.** (a) Percentage of overlap of *ZNF263* footprint sites predicted using ATAC-seq with that of *ZNF263* ChIP-seq peak sites from publicly available datasets (Imbeault et al. 2017; Pope et al. 2014; Fietze et al. 2010). The TF footprint sites are grouped by bound, unbound, or all (bound and unbound) sites. All overlaps between the predicted TF-footprint sites and ChIP-seq regions were compared against randomly selected regions and were statistically significant (hypergeometric test  $pvalue < 2.2 \times 10^{-16}$ ). (b) Enrichment of Hallmark signaling pathways in genes that are up-regulated when *ZNF263* binds to genes' promoter. (c-d) Volcano plot illustrating the genes that are activated or repressed upon *ZNF263* binding to the genes' promoter region. Each dot represents a gene. The foldchange in gene expression was calculated between groups of samples with *ZNF263* present or absent in the respective promoter region. The Wilcoxon rank sum test p-value was calculated between the two groups. The analysis was performed using the samples in (c) AR+NE- and (d) AR<sub>low</sub>NE- subtype. Note: Due to the small sample size in AR+NE+, AR-NE+, and AR-NE- subtypes, similar analyses for these subtypes were not feasible. (e) The plot illustrates the number of bound *ZNF263* footprint sites that are differentially occupied between respective mCRPC subtypes.





**Supplementary Fig. S23. *ZNF263* target gene expression.** Heatmap showing the unsupervised hierarchical clustering of (a) *ZNF263* target gene expression and (b) subset of *ZNF263* target gene that are involved in HALLMARK MYC TARGETS V1/V2 geneset.



**Supplementary Fig. S24. Association of *ZNF263* with MYC signaling pathway.** (a) Boxplot illustrating the distribution of the Spearman's correlation coefficient (R) between the gene expression profile of predicted target genes of *ZNF263* and the ATAC-seq peak accessibility where the *ZNF263* is bound. The genes were grouped into the respective enriched Hallmark signaling pathways as discussed in Figure 6b. (b) Pathway enrichment of target genes potentially regulated by both *ZNF263* and *MYC*. (c) Motif sequence logo of *MYC*, *AR* and *ZNF263*. (d) Percentage of *MYC* footprint sites that are within the vicinity of *ZNF263* footprint sites. The human reference genome was fragmented into varying bin sizes ranging from 50-1000 bp. The overlap of *ZNF263* and *MYC* footprint sites were analyzed within the above bins. Each line in the plot represents an individual mCRPC transcriptional subtype. (e) Percentage of overlap of *ZNF263* footprint sites predicted using ATAC-seq with that of *MYC* ChIP-seq peak sites from publicly available datasets (Barfeld et al. 2017; See et al. 2022; Guo et al. 2021). The TF footprint sites are grouped by bound, unbound, or all (bound and unbound) sites. All overlaps between the predicted TF-footprint sites and ChIP-seq regions were compared against randomly selected regions and were statistically significant (hypergeometric test  $pvalue < 2.2 \times 10^{-16}$ ). (f) The barplot shows the number of genes in Hallmark MYC target geneset with different combinations of *ZNF263* and *MYC* binding to the promoter region. Note: We measured 205 genes in the HALLMARK MYC TARGETS V1/V2 geneset.

## References

- Barfield SJ, Urbanucci A, Itkonen HM, Fazli L, Hicks JL, Thiede B, Rennie PS, Yegnasubramanian S, DeMarzo AM, and Mills IG, *et al.* 2017. c-myc antagonises the transcriptional activity of the androgen receptor in prostate cancer affecting key gene networks. *EBioMedicine*, **18**:83–93.
- Chen S, Huang V, Xu X, Livingstone J, Soares F, Jeon J, Zeng Y, Hua JT, Petricca J, Guo H, *et al.* 2019. Widespread and functional rna circularization in localized prostate cancer. *Cell*, **176**:831–843.e22.
- Consortium G 2013. The genotype-tissue expression (gtex) project. *Nature genetics*, **45**:580–5.
- Corces MR, Granja JM, Shams S, Louie BH, Seoane JA, Zhou W, Silva TC, Groeneveld C, Wong CK, Cho SW, *et al.* 2018. The chromatin accessibility landscape of primary human cancers. *Science (New York, N.Y.)*, **362**.
- Frietze S, Lan X, Jin VX, and Farnham PJ 2010. Genomic targets of the krab and scan domain-containing zinc finger protein 263. *The Journal of biological chemistry*, **285**:1393–403.
- Guo H, Wu Y, Nouri M, Spisak S, Russo JW, Sowalsky AG, Pomerantz MM, Wei Z, Korthauer K, Seo JH, *et al.* 2021. Androgen receptor and myc equilibration centralizes on developmental super-enhancer. *Nature communications*, **12**.
- Imbeault M, Helleboid PY, and Trono D 2017. Krab zinc-finger proteins contribute to the evolution of gene regulatory networks. *Nature*, **543**:550–554.
- Labrecque MP, Coleman IM, Brown LG, True LD, Kollath L, Lakely B, Nguyen HM, Yang YC, Costa RMD, Kaipainen A, *et al.* 2019. Molecular profiling stratifies diverse phenotypes of treatment-refractory metastatic castration-resistant prostate cancer. *Journal of Clinical Investigation*, **129**:4492–4505.
- Oki S, Ohta T, Shioi G, Hatanaka H, Ogasawara O, Okuda Y, Kawaji H, Nakaki R, Sese J, and Meno C, *et al.* 2018. Chip-atlas: a data-mining suite powered by full integration of public chip-seq data. *EMBO reports*, **19**.
- Pinskaya M, Saci Z, Gallopin M, Gabriel M, Nguyen HT, Firlej V, Descrimes M, Rapinat A, Gentien D, de la Taille A, *et al.* 2019. Reference-free transcriptome exploration reveals novel rnas for prostate cancer diagnosis. *Life science alliance*, **2**.
- Pomerantz MM, Qiu X, Zhu Y, Takeda DY, Pan W, Baca SC, Gusev A, Korthauer KD, Severson TM, Ha G, *et al.* 2020. Prostate cancer reactivates developmental epigenomic programs during metastatic progression. *Nature Genetics*, **52**:790–799.
- Pope BD, Ryba T, Dileep V, Yue F, Wu W, Denas O, Vera DL, Wang Y, Hansen RS, Canfield TK, *et al.* 2014. Topologically associating domains are stable units of replication-timing regulation. *Nature*, **515**:402–405.
- See YX, Chen K, and Fullwood MJ 2022. Myc overexpression leads to increased chromatin interactions at super-enhancers and myc binding sites. *Genome research*, **32**:629–642.
- Tang F, Xu D, Wang S, Wong CK, Martinez-Fundichely A, Lee CJ, Cohen S, Park J, Hill CE, Eng K, *et al.* 2022. Chromatin profiles classify castration-resistant prostate cancers suggesting therapeutic targets. *Science*, **376**.

Taylor BS, Schultz N, Hieronymus H, Gopalan A, Xiao Y, Carver BS, Arora VK, Kaushik P, Cerami E, Reva B, *et al.* 2010. Integrative genomic profiling of human prostate cancer. *Cancer Cell*, **18**:11–22.